Monthly Notices of the ROYAL ASTRONOMICAL SOCIETY

MNRAS **00,** 1 (2020) doi:10.1093/mnras/staa2210

High-accuracy short-term precipitable water-vapour operational forecast at the Very Large Telescope and perspectives for sky background forecast

A. Turchi [1]★ E. Masciadri [1]★ P. Pathak [2]★ and M. Kasper [2]

[1] *INAF – Osservatorio Astrofisico di Arcetri, Largo E. Fermi 5, 50125 Florence, Italy*

[2] *European Southern Observatory, Karl-Schwarzschild-Str. 2, 85748 Garching, Germany*

Accepted 2020 July 24. Received 2020 July 24; in original form 2020 May 29

ABSTRACT

In this article, we present the first results ever obtained by applying the autoregressive (AR) technique to precipitable water vapour (PWV). The study is performed at the Very Large Telescope (VLT). The AR technique was proposed recently to provide forecasts of atmospheric and astroclimatic parameters on short time-scales (up to a few hours) by achieving much better performance with respect to the 'standard forecasts' provided in early afternoon for the coming night. The AR method uses real-time measurements of the parameter of interest to improve the forecasts performed with atmospherical models. Here, we used measurements provided by the Low Humidity And Temperature PROfiling microwave radiometer (LHATPRO), a radiometer measuring the PWV at the VLT continuously. When comparing the AR forecast at 1h with the standard forecast, we observe a gain factor of ∼8 (i.e. ∼800 per cent) in terms of forecast accuracy. In the PWV $\leq$ 1 mm range, which is extremely critical for infrared astronomical applications, the RMSE of the predictions is of the order of just a few hundredth of millimetres (0.04 mm). We therefore proved that the AR technique provides an important benefit to VLT science operations for all instruments sensitive to PWV. Also, we show how such an ability to predict PWV can also be useful to predict the sky background in the infrared range [extremely appealing for Mid-infrared ELT Imager and Spectrograph (METIS)]. We quantify such an ability by applying this method to the New Earth in the Alpha Cen region (NEAR) project supported by the European Southern Observatory (ESO) and Breakthrough Initiatives.

Key words: atmospheric effects – methods: data analysis – methods: numerical – site testing.

1 INTRODUCTION

Quantification of water vapour is particularly critical for ground-based observations in the infrared spectrum (IR, submillimetric and millimetric ranges), since it is one of the atmospheric constituents that mainly affects atmospheric transmission at those wavelengths. The transmission/opacity of the atmosphere is caused mainly by the absorption of radiation from H_2O. On the other hand, water vapour is also one of the causes contributing to the sky background, due to re-emission of the absorbed energy, which impacts on the sensitivity of IR observations, and the strength of the process is dependent on the H_2O abundance in the atmosphere. The vertical distribution of water vapour in the atmosphere can be described by the vertical stratification of the mixing ratio M or the absolute humidity AH. For most practical astronomical applications, the relevant parameter is the integral of these quantities over the whole atmosphere, the so called precipitable water vapour (PWV). Forecasts of this parameter can therefore be extremely useful to optimize the potentialities and efficiency of instruments running at these wavelengths. The PWV can be forecast to support science operations by using atmospheric models, and several studies employing mesoscale models to reconstruct PWV can be found in the literature (Cucurull et al. 2000; Gonzalez et al. 2013; Giordano et al. 2013; Perez-Jordan et al. 2015; Pozo et al. 2016; Perez-Jordan, Castro-Almazan &Munoz-Tunon 2018).

In a recent article, Turchi et al. (2019) used the non-hydrostatic atmospheric model Meso-NH to forecast the PWV above Cerro Paranal (Chile), site of the Very Large Telescope (VLT), on a time-scale of 6–15 hours in the future. More precisely, the forecast of PWV for the coming night is provided early in the afternoon of the day before. A statistical analysis has been performed above Cerro Paranal, site of the VLT, on a sample of 240 nights uniformly distributed in different years (2013 and 2017) and statistical operators (bias, RMSE and σ) have been quantified in different ranges: all PWV values, PWV $\leq$ 5 mm and PWV $\leq$ 1 mm. The results of the previous analysis revealed that the proposed model and approach were extremely promising. The smaller the threshold of the interval analysed, the smaller the RMSE achieved, up to a value of RMSE = 0.27 mm in the most challenging region, i.e. when PWV $\leq$ 1 mm. This indicates that the proposed approach seems very efficient to reconstruct the most interesting values in an astronomical context, i.e. extremely low values of PWV. In the same article, we proved that the Meso-NH model provides a substantial improvement in performance (roughly a factor of 2, i.e. 100 per cent) with respect to the Atmospheric General Forecast Model of the European Centre for Medium Range Weather Forecasts (ECMWF).

More recently, a method has been proposed (Masciadri, Martelloni & Turchi 2020) aiming to improve the model performance in forecasting some relevant atmospheric and astroclimatic parameters

★ E-mail: alessio.turchi@inaf.it (AT); elena.masciadri@inaf.it (EM); Prashant.Pathak@eso.org (PP)

© 2020 The Author(s)
Published by Oxford University Press on behalf of the Royal Astronomical Society

on short time-scales (of the order of a few hours in the future, typically 1 or 2 h) using an autoregressive (AR) technique that simultaneously uses the forecast obtained with an atmospheric model on longer time-scales[1] and real-time measurement of the specific forecast parameter. Such a method has been tested successfully on the Large Binocular Telescope (LBT) and has been implemented in the Advanced LBT Turbulence and Atmosphere (ALTA) Center, the operational forecast system conceived to support science operations of this telescope. The time-scale of one hour in the future is the most critical for the queue modes of top-class telescopes, because this is the time-scale on which decisions are typically taken to switch from either one programme to another or one instrument to another.

The results of that study indicate that important gains in forecast reliability can be reached using the autoregressive approach, even if the gain (between 2.70 and 4.90 in terms of the root-mean-squared error (RMSE) reduction) depends on the specific atmospheric parameter. However, the LBT site has no real-time measurements of PWV. We still do not know, therefore, what gain in the prediction of PWV might be obtainable using this technique. The PVW is monitored nightly at the VLT with the Low Humidity and temperature PROfiling microwave radiometer (LHATPRO). This instrument has been validated by Kerber et al. (2012) and has been engineered for monitoring dry sites.

In this article, we evaluate the impact of this method on PWV at the VLT by quantifying the gain obtained in the prediction accuracy of this parameter with respect to standard forecasts (forecasts at long time-scales) and also with respect to the persistence method. The persistence method assumes that the value of a specific parameter remains equal to the value measured at the present time, t_0, for the successive hour. Increasing the forecast accuracy, even if over short time windows, can definitely help in flexible scheduling and identification of the best PWV windows to optimize infrared observations that depend critically on this parameter.

Additionally, we explore further contexts in which the forecast of the PWV might be critical and crucial. We therefore focused our attention on the New Earth in the Alpha Cen region (NEAR) project (Kasper et al. 2017), a challenging experiment promoted by ESO and Breakthrough Initiatives[2] that aims to search for exoplanets in the habitable zone (HZ) around α Centauri in the N band. Earth-type planets, with characteristics similar to our own planet, typically have orbits within [0.1–1] au of their star (red dwarf or solar type). Such planets cannot generally be detected by 8–10 m class telescopes, as we need a contrast of 10^{-5}–10^{-7} in the N band for stars within 10 pc of Earth (10^{-5} for red dwarfs and 10^{-7} for solar-type stars), but they represent an important science case for the Extremely Large Telescope (ELT). In the case of the α Centauri star system (α Centauri A and B), however, because of its proximity (1.35 pc) to Earth, the angular separation of a potential planet should be of the order of 1 arcsec and the observation of a planet in the HZ should, in principle, also be possible with 8-m class telescopes by pushing the possibile contrast and sensitivity attainable by such tools to the extreme. The concept of the NEAR project implies modification of the VLT spectrometer and imager for the mid-infrared (VISIR) instrument, which consists of combining the instrument with adaptive optics using the deformable secondary of UT4, adding a phase-mask coronograph optimized for the N band and including a new chopper system for noise filtering (Kasper et al. 2017). In the analysis presented in this contribution, we used all the NEAR project observations related to the commissioning run during the 2019 May 23–June 10 period, plus the night of 2019 June 26, for a total of 18 nights, and the entire data set related to the run performed in shared-risk basis to the community for science verification (SV), related to the 2019 December 13–19 run, for a total of 7 nights.

Table 1. Horizontal resolution of each Meso-NH imbricated domain at Cerro Paranal (VLT).

Domain	ΔX (km)	Grid points	Domain size (km)
Domain 1	10	80 × 80	800 × 800
Domain 2	2.5	64 × 64	160 × 160
Domain 3	0.5	150 × 100	75 × 50

The wavelength window between 10 and 12.5 μm, where the signal-to-noise ratio (SNR) is supposed to be maximum, has been selected. Preliminary observations performed during the commissioning seemed to indicate that PWV has an impact on the sky background, even if in principle we are in a region dominated by the telescope emission. The idea is therefore to analyse the sky background and the PWV and to establish whether we can retrieve any correlation or relation between the two quantities. This might provide new insights into the role of PWV for the instrumentation for new generation class telescopes and might eventually help us in identifying other applications of PWV forecasts.

The article is organized as follows. In Section 2, we briefly present the configuration of the numerical model used in the present study. In Section 3 we discuss the measurements provided by the VLT instrumentation. In Section 4 we briefly summarize the principles of the autoregression technique that we used to enhance the PWV forecast over a time-scale of 1 h. In Section 5 we describe the model performance obtained using the autoregression technique and compare the results obtained with the standard forecast approach and with the persistence method. In Section 6 we quantify the correlation between the sky background measured with NEAR during the commissioning and the PWV and we discuss the importance of the PWV forecast in this context. Finally, in Section 7 we present our conclusions.

2 MODEL CONFIGURATION

The atmospheric model used to forecast the atmosphere is Meso-NH[3] (MNH; Lafore et al. 1998; Lac et al. 2018). It is a non-hydrostatic mesoscale model that simulates the time evolution of a finite 3D atmospheric volume over a specific geographical area. The specific model configuration was basically the one reported in Turchi et al. (2019), thus we report here just the most relevant elements. We performed simulations over Cerro Paranal (VLT site), located at coordinates (24.62528 S, 70.40222 W) at a height of 2635 m above sea level.

We use a grid-nesting technique (Stein et al. 2000) that consists of using a set of different imbricated domains, described in Table 1, with a digital elevation model (DEM, i.e. orography) extended on smaller and smaller surfaces having a progressively higher horizontal resolution. In this way, using the same vertical grid resolution, we achieve the highest horizontal resolution on the innermost domain extended on a limited surface around the summit to provide the best possible prediction. Each domain is centred on the telescope coordinates.

[1]Typically forecasts available early afternoon for the next night.
[2]http://breakthroughinitiatives.org
[3]http://mesonh.aero.obs-mip.fr/mesonh/

The DEM used for domains 1 and 2 is the GTOPO,[4] with an intrinsic resolution of 1 km. In domain 3 we use a digital elevation model with an intrinsic resolution of 500 m (16 arcsec).

We use the the grid-nesting two-way option, which allows mutual interaction between each couple of parent and child domains, i.e. each couple of contiguous domains. The two-way configuration is known to provide more consistent and realistic results than the one-way configuration (Stein et al. 2000; Harris & Durran 2000).

We use 62 vertical levels on each domain, starting from 5 m above ground level (a.g.l.). The levels have a logarithmic stretching of 20 per cent up to 3.5 km a.g.l. From this point onward, the model uses an almost constant vertical grid size of ∼600 m up to ∼23 km, which is the top level of our domain. The grid mesh deforms uniformly to adapt to the orography, so the actual size of the vertical levels can stretch in order to accommodate the different ground level at each horizontal grid point.

In this study, we implemented the Turchi et al. (2019) model set-up in an automatic forecast system in order to run consecutively over a whole year. The system takes care of all the phases of the forecast: model initialization, data assimilation and grid configuration, parallel simulation and final post-processing phase and production of the final outputs. The system is designed in order to guarantee the delivery of the forecasts early in the afternoon before the start of the observing night. Forecasts computed in this way will be referred to as the "standard configuration" in the following sections and are the benchmark over which we will evaluate the performance of the AR method (Masciadri et al. 2020).

The model is initialized with daily operational forecasts computed by the ECMWF general atmospheric forecast model extended over the whole globe. Simulations cover night-time at VLT, which is relevant for astronomical observations on each site. The date of each simulation in this article is identified by the UT day "*J*" on which the night starts. For the Cerro Paranal case, in this study we simulate 18 hours, initializing the model at 18:00 UT of day "*J*" with ECMWF forecasts computed at 12:00 on the same day. We force the model each consecutive 6 hours with data coming from the ECMWF and we treat/analyse results in the interval [00:00–09:00] UT of day "*J*+1". This interval permits us to fit the night-time during the whole solar year.

Meso-NH computes the PWV using the vertical profiles of water-vapour mixing ratio M (kg kg^{-1}), pressure P (Pa) and temperature T (degrees K), using the following equation (1):

$$PWV = -\frac{1}{g\rho_{H_2O}} \int_{P_0}^{P_{top}} M \, dP, \quad (1)$$

where PWV is expressed in mm. In the above equation, $\rho_{H_2O} = 10^3$ kg m^{-3} is the water density and $g = 9.81$ m s^{-2} is the standard gravitational acceleration. We integrate between the ground-level pressure P_0 and the top-level (∼20 km a.g.l) pressure P_{top}. We note that the water-vapour scaleheight is in the range 1.5–2.5 km. Above the latter height, the water content decreases drastically and is typically negligible above 10 km (Querel, Naylor, Kerber 2016).

The PWV value is provided with a time sampling of two minutes of simulated time and is calculated in the innermost domain, having a horizontal resolution of 500 m. Following results obtained by Turchi et al. (2019, their equation 2), we applied the post-processing correction obtained in statistical terms, aiming to remove systematic errors of the forecast.

3 MEASUREMENTS AND INSTRUMENTATION

The instrument used as a reference in this article is the Low Humidity and Temperature PROfiling microwave radiometer (LHATPRO), which was ed at Cerro Paranal in 2011 (Kerber et al. 2012) and since then has run continuously 24/7, providing measurements stored in the ESO archive.[5] This instrument is completely automated and is manufactured by Radiometer Physics GmbH. It uses multiple microwave channels in the frequency bands 183 GHz (H_2O) and 51–58 GHz (O_2), in order to retrieve, among other things, the humidity and temperature profiles up to 10 km of altitude above the ground level. Measurements are taken at 39 vertical levels with a resolution that varies from 10 m at ground level up to 1 km at the topmost height. For a more detailed description, see Rose et al. (2005). As explained in Kerber et al. (2012), the 183-GHz line is extremely important, because it allows us to resolve the extremely low levels of PWV present on a dry site such as Paranal (the median value is around 2.4 mm).

LHATPRO was validated against radiosoundings for astronomical use in 2011 (Kerber et al. 2012), showing a good correlation with measurements, an accuracy of 0.1 mm and a precision of 0.03 mm for PWV. The instrument decreases its accuracy starting from 15 mm and starts to saturate for PWV values above 20 mm. However, these correspond to very rare bad weather events at Paranal (typically below 15 mm). In this study, we considered 15 mm as a top threshold for our analysis.

LHATPRO measures the PWV with a sample rate of 5 s, while Meso-NH samples the PWV every 2 min. In order to have a common time frame, which is fundamental in the following AR method implementation, we decided to resample both data sets over a 1-minute time step, averaging for the fast LHATPRO sample rate and interpolating over the Meso-NH slower one.

4 AUTOREGRESSIVE METHOD

One of the goals of this article is to apply the autoregressive method (Masciadri et al. 2020) to PWV at the VLT in order to quantify the gain in forecast accuracy over a short time window, which is fundamental to help the optimal planning of observations that are critically dependent on atmospheric water-vapour content in flexible scheduling. The details of the method implemented are reported in Masciadri et al. (2020) and we report a short summary here. We define a function X_t that depends on the difference between the standard configuration forecast (M) and measurements (O) calculated at time t:

$$X_t = (O_t - M_t). \quad (2)$$

The AR method allows us to predict the future value of the above function through a polynomial equation with P regressor coefficients a_i:

$$X_{t+1} = \sum_{i=1}^{P} a_i (O_{t-i+1} - M_{t-i+1}). \quad (3)$$

The a_i regressors are computed through a least-mean-squares minimization over a finite number N of past nights, then the AR PWV prediction A is obtained as $X^*_{t+1} = M_{t+1} + X_{t+1}$.

At each time t during the night, all the measurements for $t' \leq t$ and all standard configuration predictions until of the end of the night are available. In order to perform a prediction over L hours in the

[4] https://lta.cr.usgs.gov/GTOPO30

[5] http://www.eso.org/asm/ui/publicLog?name=Paranal

future, we advance the time series X^* for one hour in the future, then we again update the regressor coefficients, adding the AR predicted values between t and $t+1$ sequentially to the measurements collected until time t. This is done in order to contain the AR divergence from the measurements. We then repeat the above prediction.

We used the same approach described in Masciadri et al. (2020) and applied to Mount Graham, site of the Large Binocular Telescope, i.e. the AR is computed each hour with the same number of regressors (50) and using the same number of nights in the past ($N = 5$). As explained in the previous article, it has been observed that the gain of the AR with respect to the standard forecast, in terms of RMSE reduction, is often grater than 1 even after 4 hours in the future. In this article, we extended the estimate of the RMSE as a function of ΔT (the time in the future from any given present time) up to 6 hours. We only consider night-time and, for any date "J", we do not have standard forecast data before 18:00 UT; moreover the method can only run successfully if there is at least an hour of measurements that overlaps with the standard prediction starting from X_t backward, so the AR forecast cannot start before 19:00 UT on each day. If the previous condition is not met, we assume automatically that we do not have enough data to perform the AR prediction.

Within the previous constraints, we notice that the larger ΔT, the smaller the sample on which one can compute the statistics. In other words, the sample on which RMSE is computed at $\Delta T = 1$ h is richer than that on which is computed at $\Delta T = 6$ h.[6]

To produce the AR forecasts, we updated the automatic system described in Section 2 by adding the AR method, again simulating regular operations, using the real-time measurements available at the VLT. The aforementioned exercise allowed us to validate the automatic forecast implementation successfully and obtain a large set of simulations over a whole year at Cerro Paranal.

5 RESULTS

In this section, we aim to quantify the performance of the AR method explained in Section 4. The AR method requires a continuous sample of simulated nights to work efficiently, due to the need for a buffer of past nights over which to compute the autoregressor coefficients. For this reason, we considered a total sample size of 365 nights between 2018 August 1 and 2019 July 31 (UT). On 10 nights we could not run the AR method due to missing data, so the final sample size used in the analysis is 355 nights. We performed the analysis in terms of classical statistical operators RMSE, σ and bias and scatter plots between measurements and forecasts in both configurations (standard and AR), in order to compare the different forecast accuracies of the two methods.

In order to be consistent with previous studies of PWV at Cerro Paranal (Turchi et al. 2019) and the study carried out with the AR method (Masciadri et al. 2020), we performed a 20-min resampling over both measurements and predictions (standard configuration and AR) before computing the statistical operators and the scatter plots. The main reason behind this is to filter out the high frequencies and collect evidence of the forecast trend, which is the most relevant information from the user's point of view.

Considering that the median value of PWV over Cerro Paranal is 2.5 mm, as reported in Fig. A1, we divided the sample into three ranges: the first takes into consideration all PWV values below 15 mm, which accounts for almost all the PWV values registered over Cerro Paranal and, as explained in Section 3, is the value range in which the instrument is most accurate; the second range takes into account all PWV values below 5 mm, which includes the most common PWV values; the third range considers all PWV values below 1 mm, which are to be considered rare extremely low PWV events in which water is almost absent from the vertical column over the telescope and can effectively allow observations practically unobstructed by water absorption. In the sample analysed in this study, we calculated that this corresponds to 8 per cent of the total PWV measured values. In Appendix A, we repeated the analysis on the last five years and verified that the percentage of cases in which PWV $\leq$ 1mm is of the order of 5–10 per cent, therefore the statistics of the sample analysed in this study are reliable. The relative rarity of these extremely low PWV values clearly shows the benefit of an accurate model forecast in order to take advantage of low PWV time windows as soon as they appear. The statistical analysis was performed over all three different ranges.

In Fig. 1, first row, we show the scatter plots obtained by comparing MNH outputs (standard configuration), which serve as a reference for this study, with measurements in the three PWV ranges. Statistical indicators are also reported in Table 2 (top). The results of the same analysis performed on AR forecasts extended 1 hour in the future are reported in Table 2 (bottom), associated with the respective gains with respect to the standard forecast (Fig. 1, bottom) reported in parentheses. We see, by comparison with the standard configuration results, that the correlation between AR prediction and measurements is significantly enhanced. The RMSE is in the range [0.13–0.04 mm], which is comparable with or even below the accuracy of the LHATPRO instrument itself (which Kerber et al. 2012 reported to be $\sim$0.1 mm[7] and is computed with respect to the measured value.). By looking at Table 2, results show that the AR prediction we implemented provides a considerable gain on a time-scale of 1 h with respect to the standard forecast. The maximum gain is 8.38 and that for PWV $\leq$ 1 mm is 8.25. The ability to predict rare extremely low PWV events with negligible discrepancy from the measured value (0.04 mm RMSE) is extremely helpful in observation scheduling at VLT.

Following the same scheme used in Masciadri et al. (2020), in Fig. 2 we report the RMSE obtained by applying the AR method over different forecast time-scales, from 1–6 hours in the future. The horizontal black line corresponds to the RMSE error obtained with the MNH model forecast from the day before, while the coloured lines correspond to the AR forecast performed with an increasing number of past nights used in AR coefficient computation (from 1–5). As expected, we observe that the AR forecast accuracy tends to decrease with a longer forecast time-scale in the future, becoming similar to the mesoscale MNH forecast (standard configuration). The gain factor is still relevant (still a 30 per cent reduction in the RMSE) up to 3 hours in the future and tends to become negligible after 6 hours. It is interesting to observe that results published in Masciadri et al. (2020) relative to other atmospheric parameters (temperature, relative humidity, wind speed and direction) reported a maximum gain of 4.9, while in this study we observe a much higher factor of gain for PWV in terms of RMSE reduction (almost double). Of course, we cannot state, at the present time, if this is due to the different site (Mount Graham versus Cerro Paranal) or the nature of the parameter itself.

For completeness, we remember that the scattering plots related to the standard forecast have been calculated here only to be able

[6]Both samples remain in any case statistically significant.

[7]Of course the instrument accuracy is valid for all reported PWV values, while the forecast accuracy of 0.04 mm is for PWV $\leq$ 1 mm.

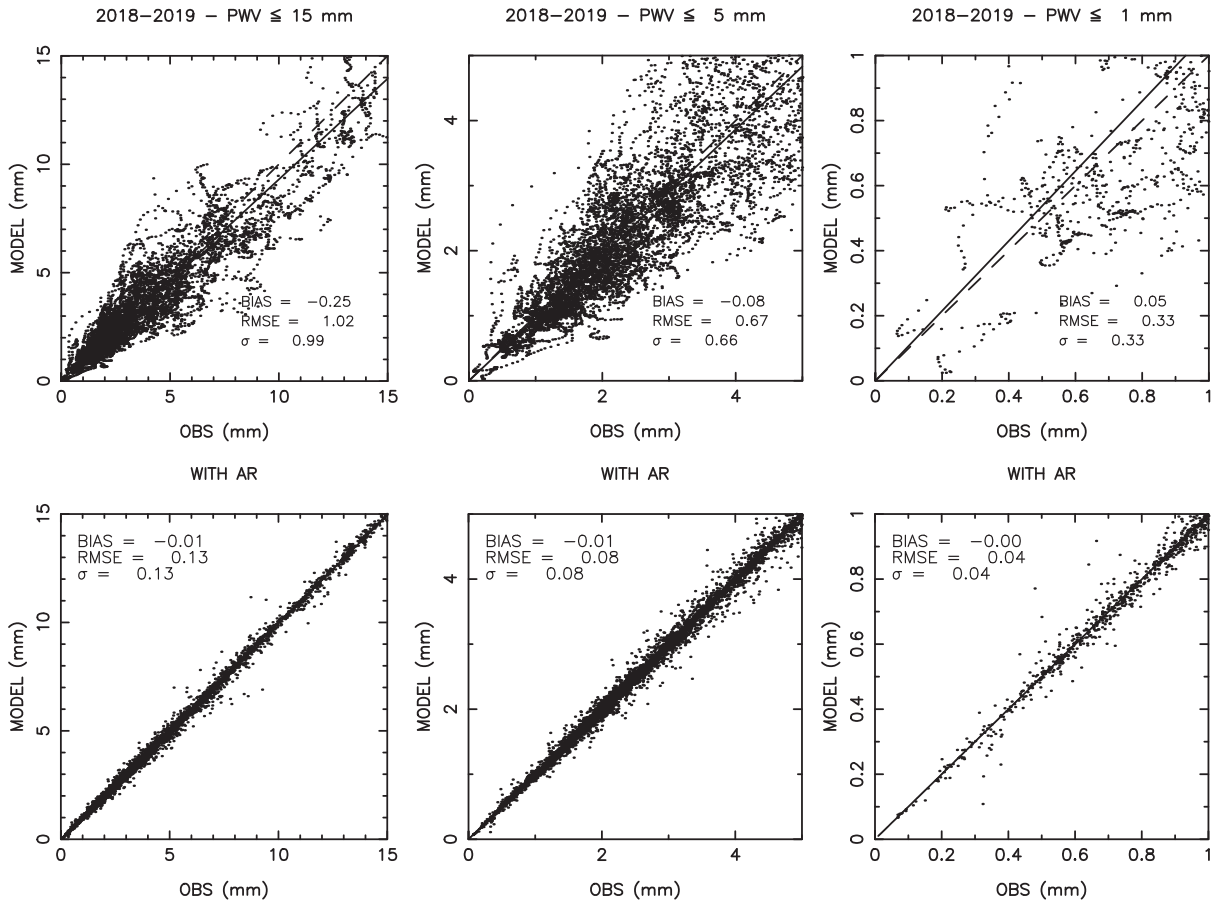

Figure 1. First row: scatter plots computed between forecasts and observations on the whole sample of nights (355). In the first row, the forecasts in the standard configuration are shown, in the second row the results obtained with the AR method on a time-scale of 1 hour. The statistical operators are calculated in three different ranges: PWV $\leq$ 15 mm (left), PWV $\leq$ 5 mm (centre) and PWV $\leq$ 1 mm (right). The straight line corresponds to the regression line computed on the data points.

Table 2. In each column we show the statistical indicators computed over the 355-night sample considered in this study. The indicators are computed on a sample filtered by selecting LHATPRO measurements with a PWV $\leq$ 15 mm sample, a sample with PWV $\leq$ 5 mm and a sample with PWV $\leq$ 1 mm. We present values computed first using the standard configuration forecast, then using the enhanced AR forecast extended 1 hour in the future. In the latter case, in parentheses, we report the gain factor with respect to the standard configuration for the specific statistical indicator.

	RMSE (mm)	BIAS (mm)	σ (mm)
	Standard configuration		
All PWV	1.02	− 0.25	0.99
PWV $\leq$ 5 mm	0.67	− 0.08	0.66
PWV $\leq$ 1 mm	0.33	0.05	0.33
	AR 1h forecast		
All PWV	0.13 (7.85)	− 0.01 (24.0)	0.13 (7.62)
PWV $\leq$ 5 mm	0.08 (8.38)	− 0.01 (8.0)	0.08 (8.25)
PWV $\leq$ 1 mm	0.04 (8.25)	0.00 (NA)	0.04 (8.25)

to quantify the gain of the AR method. A dedicated study on the standard forecast of PWV at VLT has been performed by Turchi et al. (2019). We refer the reader to that article for details. We just observe that results found here are perfectly consistent. The small differences in the statistical operators (bias, RMSE and σ) are due to the fact that the samples are not the same. It is important to note that, in the case of Turchi et al. (2019), in order to analyse the window PWV $\leq$ 1 mm, the authors enriched the sample size in the low PWV range by including extra nights in which PWV $\leq$ 1 mm has been observed to obtain a more significant statistical sample, finding RMSE = 0.25 mm. We cannot do the same in this study, as we are forced to select consecutive dates due to the AR method requirements. The enrichment cannot therefore be replicated in the same way.

Also, from Fig. 2 it is evident that the AR performance increases with the number of past nights considered (N) in the AR coefficient computation, even if in a less important way than is observed in the study performed at Mount Graham for other atmospheric parameters (Masciadri et al. 2020). The improvement in performance is absent on a time-scale of 1 hour and becomes very small for $N \geq 3$. In applying this method to an operational forecast setup for Cerro Paranal, we can, however, use $N = 5$, as the computational cost between 3 and 5 nights buffer is not relevant. As expected, the mesoscale forecast tends to be more efficient on longer time-scales and also has the advantage of being available early in the afternoon for the telescope planning. This comparison, however, explains clearly the need for different forecast schemes depending on the different use cases. For PWV, the AR forecast is advantageous with respect to the standard one for time-scales up to around 6, assuming that the night has already started.

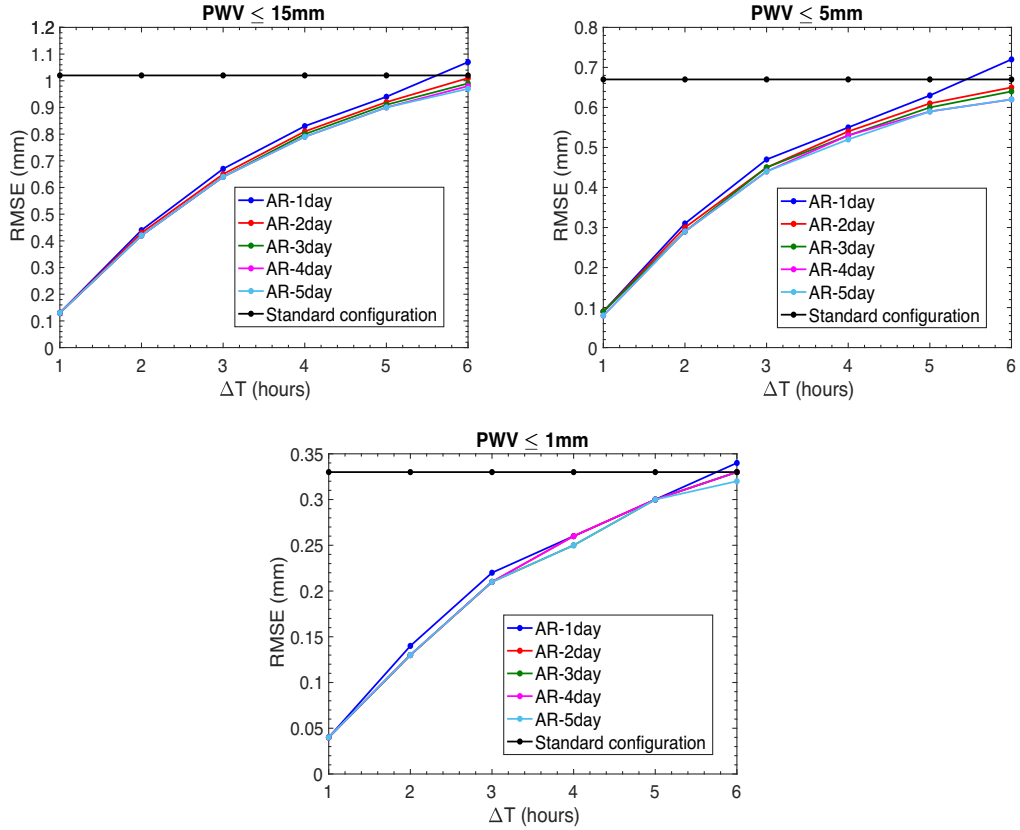

Figure 2. RMSE obtained for the AR method with respect to different forecast times (ΔT) from 1–6 hours and with different buffer sizes (different colour curves). The black line is the reference RMSE obtained with MESO-NH standard forecasts. The RMSE is computed over the PWV $\leq$ 15 mm sample (top left), the PWV $\leq$ 5 mm sample (top right) and the PWV $\leq$ 1 mm sample (bottom centre).

Fig. 3 shows a comparison of the AR method with the method of persistence. The latter forecast method assumes that, at each full hour as in the AR case, we can forecast the future values of PWV by considering the present PWV value as constant, i.e. assuming that PWV will not change in the successive 1–6 hours. We observe that the persistence method clearly loses against the AR method in all configurations. Moreover, as in the AR method case, the persistence forecast method decreases in performance with forecast time (ΔT), but it becomes worse than the standard forecast well before than the AR method, i.e. after only 3–4 hours. This is particularly evident for the PWV $\leq$ 1 mm case. In the latter case, the performance scaling of the persistence method is more irregular than in the other two cases; however, this may be due to the fact that the statistics for this particular sample are lower with respect to the other two cases. We conclude therefore that, even if the forecast by persistence introduces some improvements in forecast performance at short time-scales with respect to the standard forecast, the AR method definitively provides much better performance (a factor of 2–3 better) with respect to the method of persistence. These results are consistent with those found for other atmospheric parameters above Mount Graham (Masciadri et al. 2020).

To illustrate the capabilities of the AR forecast in reconstructing the short-time PWV predictions correctly, we report some practical examples here. Fig. 4 shows a few examples associated with extremely low PWV events. The time evolution of the AR forecast is reconstructed by joining all the 1-hour forecasts performed at each hour during the night sequentially. In this figure, we can appreciate that the standard forecast is already quite close to the observations, but the AR method is able to improve the forecast accuracy in a non-negligible way. The AR prediction helps in correcting small systematic errors, e.g. in the 2018 September 21 case, in situations where the standard forecast predicts the PWV evolution trends correctly. In other cases, e.g. 2018 November 12 and 2019 June 1, the AR prediction can anticipate rapid drops in PWV value, giving a clear advantage in programme-switching of the telescope during the observing night. Specifically, on night 2019 June 1, the standard prediction lags behind by $\sim$2 hours with respect to the measurements and the AR is very efficient in correcting this temporal shift. The most interesting case is the night 2019 May 23, where the AR forecast was able to reconstruct an extremely rare low PWV event (PWV = 0.1 mm) lasting for 4 hours, which basically allows for ground observations completely unobstructed by atmospheric water.

Fig. 5 shows, in contrast, some examples in which the standard forecasts show a larger deviation from the measured PWV values. In these cases, the model may either present large biases with respect to the measurements or be unable to predict events in which the PWV value changes unexpectedly due to unpredictable weather fluctuations. In these situations, the AR forecast also helps in correcting these large discrepancies and recovering an accurate forecast and trend reconstruction in an extremely efficient way. The AR forecast is indeed able to correct the model prediction and reconstruct the evolution of PWV, even in the presence of large fluctuations where PWV varies by 4–5 mm in 2–3 hours (e.g. 2019 January 12). This level of performance allows for an extremely accurate observation scheduling, which saves observing time and

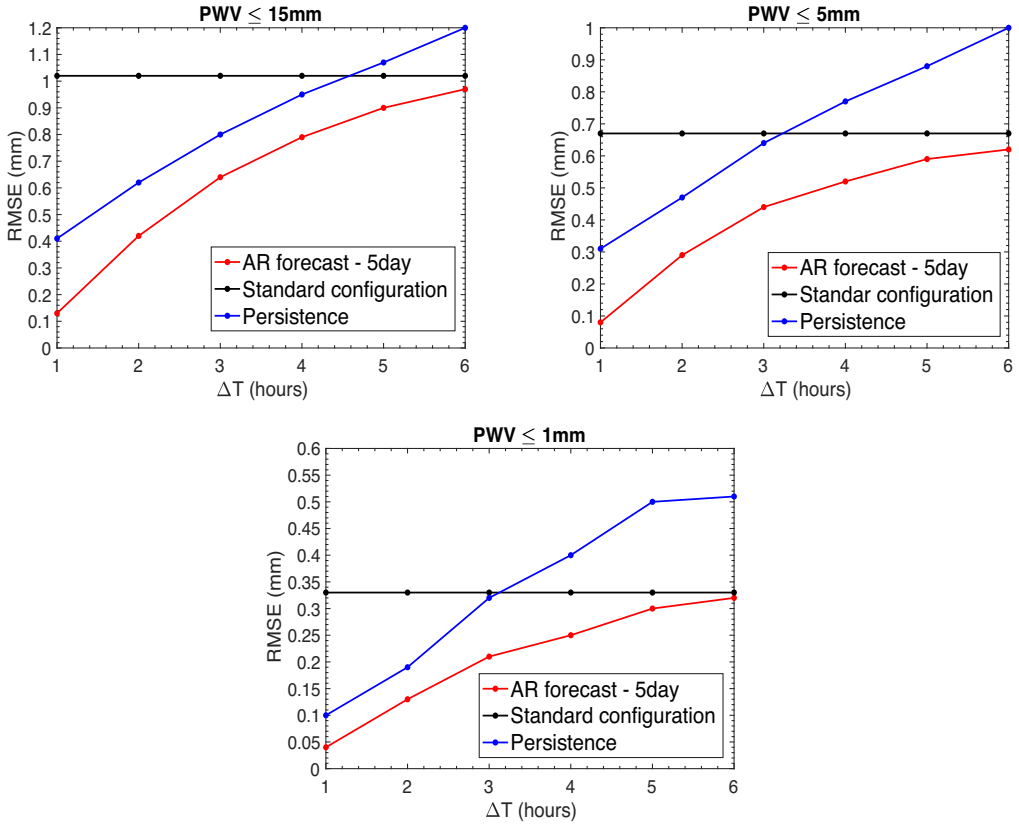

Figure 3. RMSE obtained for the persistence method (blue line) and the AR method (red line) for different forecast times ΔT from 1–6 hours. The black line is the reference RMSE obtained with the MESO-NH standard forecast. In the AR method, $N = 5$. The RMSE is computed over the PWV $\leq$ 15 mm sample (top left), the PWV $\leq$ 5 mm sample (top right) and the PWV $\leq$ 1 mm sample (bottom centre).

optimizes the throughput of scientific programmes critically dependent on PWV.

Results obtained in this study greatly improve our ability to reconstruct the PWV in advance, with potential important consequences in terms of the efficiency of the queue mode managing of top-class telescopes such as the VLT. Such a high level of reliability in the PWV forecast would be useful for all instruments of the VLT running in the IR, submillimetric and millimetric ranges. We therefore consider the VLT Imager and Spectrometer for the mid-Infrared (VISIR; Lagage et al. 2004), which operates in the (5–20 μm) range. At the same time, this could be useful for a set of other instruments running at shorter wavelengths (visible or near-infrared) that benefit from a low value of PWV, such as CRyogenic InfraRed Echelle Spectrograph (CRIRES; Kaeufl et al. 2004), X-SHOOTER (Vernet et al. 2011), Multi-Unit Spectroscopic Explorer (MUSE; Henault et al. 2003) and VLTI GRAVITY (Eisenhauer et al. 2008).

6 NEAR PROJECT: SKY BACKGROUND

In this section, we present an application of the PWV forecast to the NEAR IR project which was run at VLT, as explained in Section 1, operating in the 10–12.5 µm wavelength range. As reported in Kasper et al. (2017), a new spectral filter has been implemented in NEAR to maximize the signal-to-noise ratio (SNR). The selection of the bandpass is the result of a compromise. On one hand, it should be interesting to go towards a wide bandpass to increase the number of photons collected. On the other hand, it should be preferable to ignore some parts of the spectrum. More precisely, below 10 µm the sky background increases (Kasper et al. 2017, their fig. 4) and the absorption from ozone O_3 diminishes the atmospheric transmission. Above 12.5 µm, absorption from CO_2 becomes an important limitation for the observations. In the context of the NEAR project, therefore, the band [10–12.5] µm has been selected. In this band, the background is dominated by the telescope emission and sensitivity to other atmospheric conditions is weak, thus the PWV value is one of the main elements left that must be accounted for.

We first analysed the data set related to the commissioning period to compute the correlation between sky background counts and PWV. Observations have been carried out with an angular groove phase mask coronograph (AGPM) optimized for the N band. The AGPM is a variation of a vortex coronagraph with very small inner working angle and high throughput (Mawet et al. 2005). We considered the following technical specifications: an exposure time DIT = 6 msec, $\Delta\lambda = 2.5$ µm, pixel scale = 0.045 arcsec, efficiency = 0.1 (including the instrument transmission and the telescope reflectivity) and GAIN = 20. To pass from counts to physical quantities, we took into account a bias of the system of 10 kcts. This led to Fig. 6, where blue dots represent the scattering plot between the sky background and the observed PWV. We note that, as expected, the sky background in the [10–12.5] µm window is coherent with that shown in Kasper et al. (2017, their fig. 4) in terms of order of magnitude of the emission, which is mainly below 0.5–0.6 $\times$ 10^9 photon s^{-1} m^{-2} μm^{-1} $arcsec^{-2}$.

The interesting result is, however, that it is possible to observe a general correlation between sky background and PWV, which seems to be valid over a wide range of PWV values from

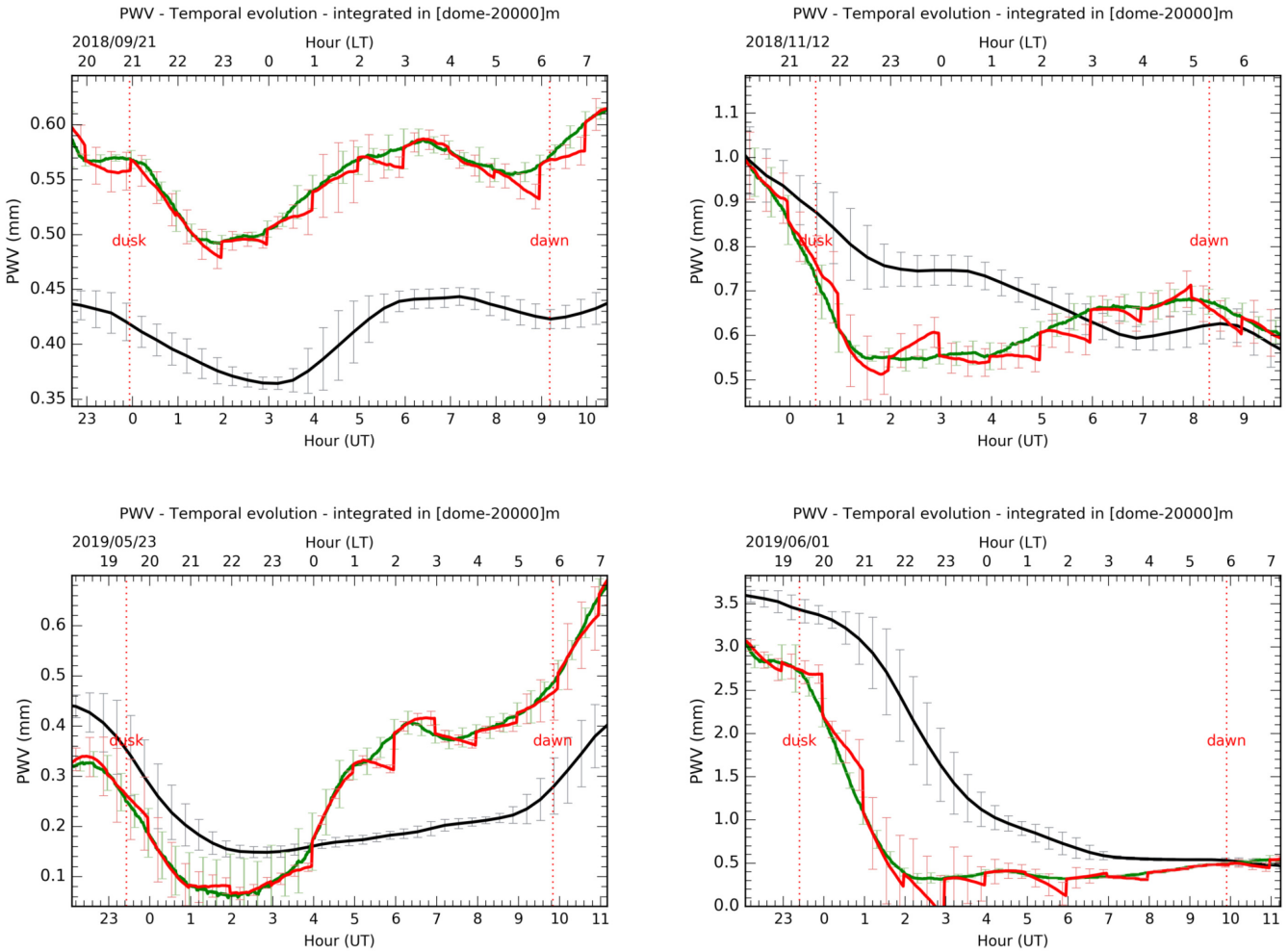

Figure 4. Time evolution of PWV during a few test nights with low PWV events. The black line shows the standard forecast, the green line shows the observations and the red line shows the forecast with the AR method on a 1-h time-scale. The time evolution of the AR forecast is reconstructed by aligning sequentially all the 1-hour forecasts performed each hour during the night. The error bars represent the variability of PWV during a 20-min interval. The date of each figure corresponds to the start of the night at VLT. The top x-axis is the local time (LT), while the bottom x-axis is time in UT. The times corresponding to dawn and dusk are shown in each figure by the red dotted vertical lines.

0–7 mm. The spikes around PWV = 2 mm might be explained by emission due to some molecular absorption lines or interaction with dust in the atmosphere, as described in Kasper et al. (2017, their fig. 4). The contribution to these few peaks around PWV = 2 mm comes from different observations on different nights, so it cannot be related to an isolated case and is therefore probably realistic.

The evidence of a sky background dependence on PWV is supported by the fact that the cold Lyot stop blocks emission from the room-temperature telescope environment (central obscuration, M2 support structures, etc). This leaves only blackbody radiation from the warm telescope mirrors and the cryostat entrance window, which should be comparable to the sky emission (see Kasper et al. 2017). The point at which the dashed black line intersects the y-axis gives an indication of the telescope emission attenuated by the Lyot stop. The value of intersection with the y-axis is of the order of 0.37×10^9, which is somewhat lower than estimated by Kasper et al. (2017: $\sim 0.6 \times 10^9$).

After the first analysis was completed, we also considered the data set of the science verification (SV) to enrich the statistics, taking care to normalize with respect to the same observational conditions. During the SV, a different Lyot stop has been used with respect to the commissioning run (NEAR-201 versus NEAR-101), permitting a larger throughput for signal and sky background (93 per cent instead of 75 per cent). Emission therefore has to be corrected by a factor of 75/93 compared with the commissioning data set. The red squares in Fig. 6 show results obtained with the SV data set. We can see that results with both data sets are quite consistent, the general correlation between the emission and the PWV is confirmed and the regression line is changed only slightly by the addition of SV data. Specifically, the coefficients of the $y = ax + b$ regression line change from [$a = 3.10 \times 10^7$, $b = 3.73 \times 10^8$], obtained with the commissioning data only, to [$a = 3.18 \times 10^7$, $b = 3.72 \times 10^8$], obtained using the whole dataset. We also verified that the NEAR data are consistent with the sky background increase with PWV predicted by ESO's SKYCALC tool.[8] The crosses in Fig. 6 show the predicted values assuming a total mirror and warm side of the cryostat emissivity of 7 per cent and an instrument transmission of 50 per cent.

[8] http://www.eso.org/sci/software/pipelines//skytools/skycalc

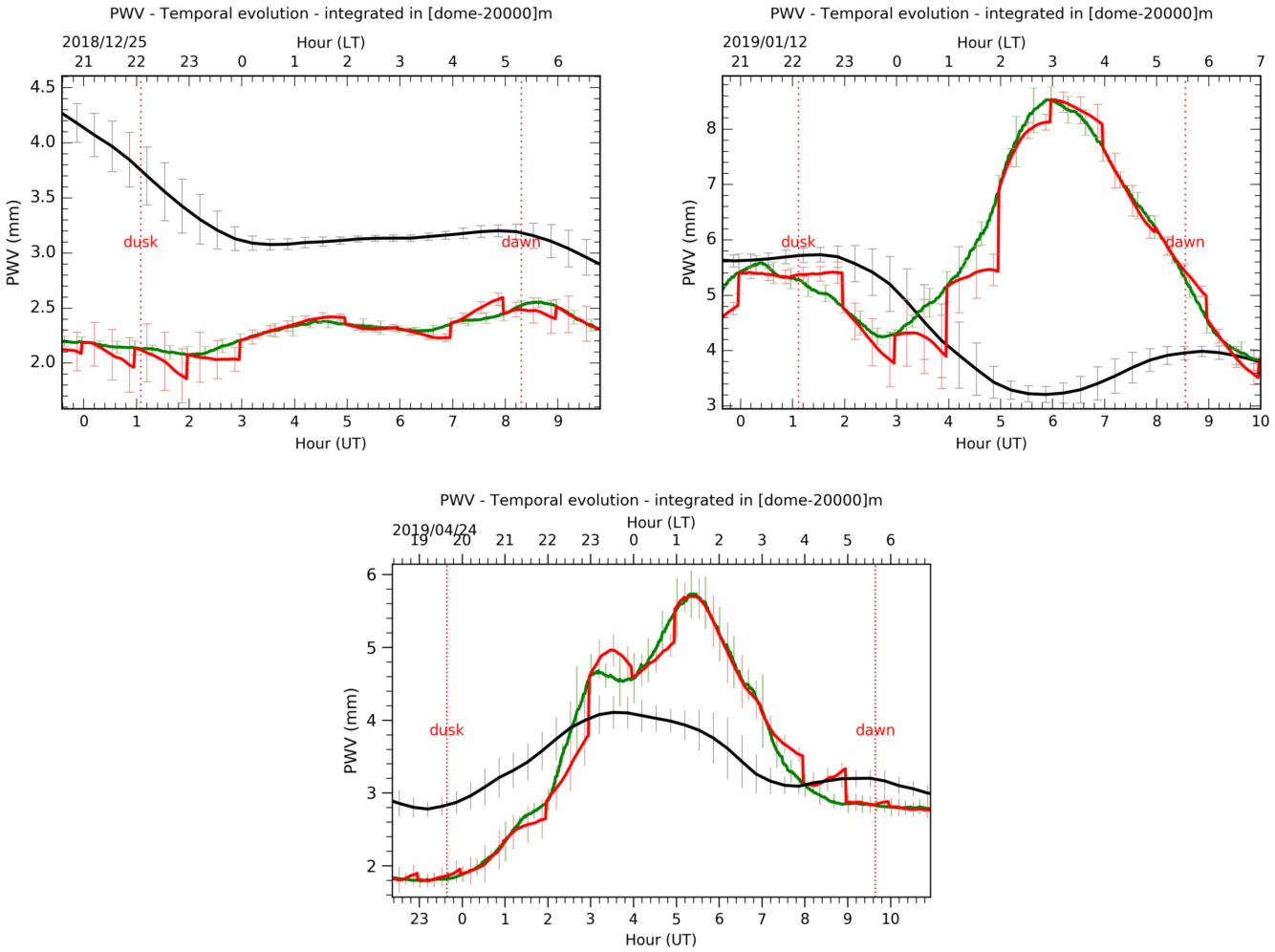

Figure 5. As Fig. 4, but the logic of the selection has been to identify a few test nights where the AR forecast is able to correct discrepancies between standard forecasts and the observations.

The important conclusion is therefore that knowledge of PWV in advance can provide indirect information about sky-background regimes, allowing identification of conditions with an optimal sky background for the most challenging observations. As we have shown in this article, PVW can be quantified in a very accurate way on a time-scale of a few hours, thus our results indicate that it is indeed possible to predict the order of magnitude of the sky background.

At the same time, this analysis provides evidence that the correlation between sky background and PVW seems to be an important element to take into account in the design and realization of METIS,[9] a first light instrument conceived for the European Extremely Large Telescope (E-ELT; Stuik et al. 2016).

7 CONCLUSIONS

In this study we aim to improve PWV forecasts on short time-scales using a method recently proposed for this goal, to be applied to atmospheric and astroclimatic parameters (Masciadri et al. 2020). The goal of the study is to analyse the impact of this strategy on the PWV at Cerro Paranal, site of the VLT, and in particular the implications in terms of science operations. This method is based on an autoregressive technique. It makes use of forecasts extended on a long time-scale, performed in our case with a mesoscale model (we call this the 'standard forecast') and computed in advance, and real-time measurements obtained by the telescope instrumentation. In this article we have shown that this method increases the accuracy of PWV forecasts significantly, by a factor that can be as high as ∼8.38 on a time-scale of 1 h. This means a gain of ∼800 per cent. Results obtained above Mount Graham, analysing other atmospheric parameters and seeing, revealed consistent gains, but not as high as the one obtained for PWV in this study.

More precisely, we proved that, in extremely low PWV regimes (PWV $\leq$ 1 mm), which are the most interesting for ground-based IR astronomy, the forecast accuracy of our method achieves a negligible error (RMSE $\sim$ 0.04 mm) with respect to the measurements for forecasts on a time-scale of 1 hour. The RMSE is slightly larger (the gain decreases in intensity if we consider larger time-scales: 2 h, 3 h, etc.), but remains advantageous with respect to the standard forecast, up to around 6 hours in the future. We also proved that the method was revealed to be much better performing than the forecast by persistence, which takes into account only real-time measurements. Accuracies are still extremely good for different PWV categories. For PWV $\leq$ 15 mm, we obtain RMSE = 0.13 mm, while for

[9]METIS = Mid Infrared ELT Imager and Spectrograph.

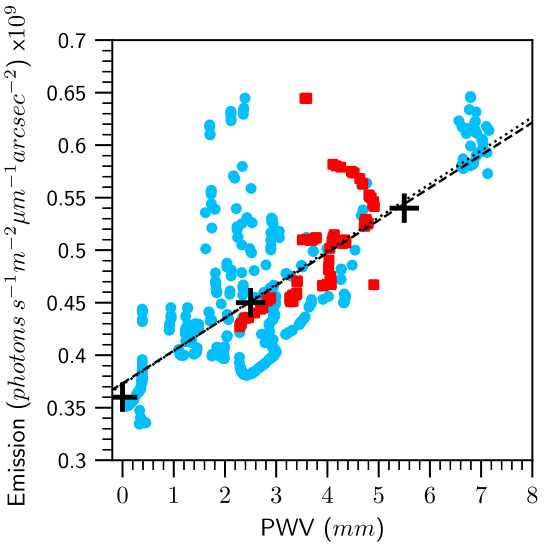

Figure 6. Relation between emission from sky background obtained with the VISIR instrument in the NEAR experiment and the observed PWV from LHATPRO. Blue dots represent data obtained with the commissioning data set (419 points), red squares are from the SV data set (101 points). The dashed line is the linear regression computed only for the commissioning data. The dotted line is computed for all data from both commissioning and SV data sets. The crosses represents the values obtained with ESO's SKYCALC tool.

PWV $\leq$ 5 mm we obtain RMSE = 0.08 mm. By knowing that the accuracy of the measurements is 0.1 mm, we can conclude that we have basically achieved at least the limit of the instrumental accuracy with forecasts on a 1-h time-scale for all cases: PWV $\leq$ 15 mm, PWV $\leq$ 5 mm and PWV $\leq$ 1 mm.

The standard forecast is still essential to long-term planning. Also, of course, it it plays a role in the accuracy of the AR method. We implemented such a method in an automatic tool in order to assess its reliability for potential operational support of VLT observations.[10] Results obtained in this study clearly indicate that such a system can definitely play an important role in VLT observation scheduling and can improve scientific throughput of critical IR observational campaigns.

Besides this, we tested our system during the NEAR project commissioning and science verification and discussed a potential further application of the PWV forecast. This has been done using the NEAR project commissioning and science verification data set related to a total sample of 25 nights. We found that the PWV values are directly correlated with sky-background IR emission in the [10–12.5] μm wavelength window in which the NEAR project runs, which is the optimal window in which molecular absorption from other atmospheric constituents is minimal. This evidence tells us that knowledge in advance of PWV can be considered an indirect estimate of the sky background and this might open further applications of PWV forecasts. Of course, it would be nice to confirm these results with a richer statistical sample.

The ability to predict PWV accurately, and thus to have an indirect prediction of the sky-background emission, could have a positive impact on IR observations and on the exploitation of next-generation ELT IR instruments such as METIS.

[10]At this stage this is not an official ESO forecast system.

ACKNOWLEDGEMENTS

The authors thank the NEAR experiment team for giving access to the sky background measurements. The authors also thank Filippo Mannucci for useful discussions. This research has received funding from the European Union's Horizon 2020 research and innovation programme under grant agreement No 824135 (SOLARNET). Initialization data come from the HRES atmospheric general forecast model of the ECMWF.

DATA AVAILABILITY

Model initialization data come from ECMWF atmospherical general forecast model HRES.[11] All NEAR project data are publicly available without restriction from archive.eso.org.[12] The data produced by the model simulations can be shared on reasonable request to the corresponding author.

REFERENCES

Cucurull L., Navascues B., Ruffini G., Elósegui P., Rius A., Víla J., 2000, J. Atmos. Ocean. Technol., 17, 773
Eisenhauer F. et al., 2008, ESO Astrophys. Symp., 41, 431
Giordano C., Vernin J., Vazquez Ramio H., Munoz-Tunon C., Varela A. M., Trinquet H., 2013, MNRAS, 430, 3102
Gonzalez A., Exposito F. J., Pereze J. C., Diaz J. P., Taima D., 2013, Q. J. R. Meteorol. Soc., 139, 2119
Harris L. M., Durran D. R., 2010, Mon. Weather Rev., 138, 2174
Henault F. et al., 2003, Proc. SPIE, 4841, 1096
Kaeufl H. U. et al., 2004, Proc. SPIE, 5492, 1218
Kasper M. et al., 2017, The Messenger, 169, 16
Kerber F. et al., 2012, Proc. SPIE, 8448, 84463N
Lac C. et al., 2018, Geosci. Model Dev., 11, 1929
Lafore J.-P. et al., 1998, Annales Geophysicae, 16, 90
Lagage P. O. et al., 2004, The Messenger, 117, 12
Masciadri E., Martelloni G., Turchi A., 2020, MNRAS, 492, 140
Mawet D., Riaud P., Absil O., Surdej J., 2005, ApJ, 633, 1191
Perez-Jordan G., Castro-Almazan J. A., Munoz-Tunon C., Codina B., Vernin J., 2015, MNRAS, 452, 1992
Perez-Jordan G., Castro-Almazan J. A., Munoz-Tunon C., 2018, MNRAS, 477, 5477
Pozo D., Marin C., Illanes L., Cure M., Rabanus D., 2016, MNRAS, 459, 419
Querel R. R., Naylor D. A., Kerber F., 2016, PASP, 123, 222
Rose T., Crewell S., Loehnert U., Simmer C., 2005, Atmos. Res., 75, 183
Stein J., Richard E., Lafore J. P., Pinty J. P., Asencio N., Cosma S., 2000, Meteorol. Atmos. Phys., 72, 203
Stuik R. et al., 2016, Proc. SPIE, 9909, 99090B
Turchi A., Masciadri E., Kerber F., Martelloni G., 2019, MNRAS, 482, 206
Vernet J. et al., 2011, A&A, 536, A105

APPENDIX A: CERRO PARANAL CLIMATOLOGY

We report here the cumulative distributions of PWV obtained with the 355-night sample from 2018/2019 used in the present study (Fig. A1, red line). This is coherent with the statistics published in Turchi et al. (2019), which treated data in the years 2013 and 2017. For the sake of completeness, we also report the cumulative distribution of the PWV values at Cerro Paranal from 2015 April 28, which is the earliest LHATPRO measurement available in the ESO database, to

[11]https://confluence.ecmwf.int/display/FUG/12.D++Model+Information
[12]http://archive.eso.org/eso/eso_archive_main.html

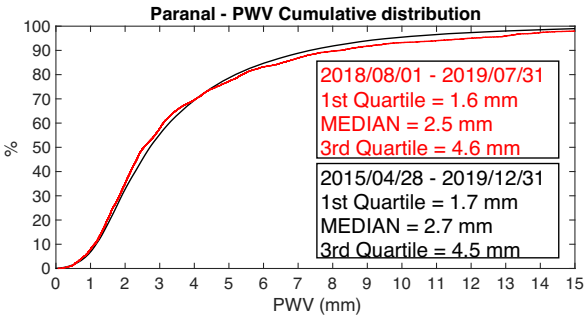

Figure A1. Cumulative distribution of PWV over the 355-night sample from 2018/2019 (red) used in this study and for the five years 2015–2019 (black), as measured by LHATPRO.

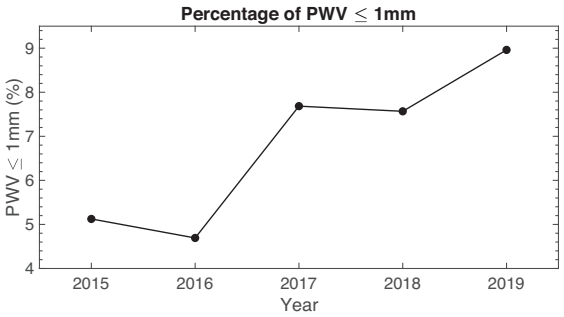

Figure A2. Evolution of the percentage of time with PWV $\leq$ 1 mm at Cerro Paranal between 2015 and 2019, with respect to the total PWV observations in each year.

2019 December 31 (Fig. A1, black line). We observe that the chosen sample for this study is quite representative of the whole global sample. In Fig. A2 we report the evolution of the percentage of time at Paranal characterized by extremely low PWV values $\leq$1 mm, with respect to the total PWV observations in each year between 2015 and 2019. While the number of years monitored by LHATPRO is still low for a proper climatological analysis, it is enough to conclude that we can expect a percentage of extremely low PWV events in the range of 5–10 per cent of the total time each year.

This paper has been typeset from a TEX/LATEX file prepared by the author.

List of astronomical key words (Updated on 2020 January)

This list is common to *Monthly Notices of the Royal Astronomical Society, Astronomy and Astrophysics*, and *The Astrophysical Journal*. In order to ease the search, the key words are subdivided into broad categories. No more than *six* subcategories altogether should be listed for a paper.

The subcategories in boldface containing the word 'individual' are intended for use with specific astronomical objects; these should never be used alone, but always in combination with the most common names for the astronomical objects in question. Note that each object counts as one subcategory within the allowed limit of six.

The parts of the key words in italics are for reference only and should be omitted when the keywords are entered on the manuscript.

General
editorials, notices
errata, addenda
extraterrestrial intelligence
history and philosophy of astronomy
miscellaneous
obituaries, biographies
publications, bibliography
sociology of astronomy
standards

Physical data and processes
acceleration of particles
accretion, accretion discs
asteroseismology
astrobiology
astrochemistry
astroparticle physics
atomic data
atomic processes
black hole physics
chaos
conduction
convection
dense matter
diffusion
dynamo
elementary particles
equation of state
gravitation
gravitational lensing: micro
gravitational lensing: strong
gravitational lensing: weak
gravitational waves
hydrodynamics
instabilities
line: formation
line: identification
line: profiles
magnetic fields
magnetic reconnection
(magnetohydrodynamics) MHD
masers
molecular data
molecular processes
neutrinos
nuclear reactions, nucleosynthesis, abundances
opacity
plasmas
polarization
radiation: dynamics
radiation mechanisms:general
radiation mechanisms: non-thermal
radiation mechanisms: thermal
radiative transfer
relativistic processes
scattering
shock waves
solid state: refractory
solid state: volatile
turbulence
waves

Astronomical instrumentation, methods and techniques
atmospheric effects
balloons
instrumentation: adaptive optics
instrumentation: detectors
instrumentation: high angular resolution
instrumentation: interferometers
instrumentation: miscellaneous
instrumentation: photometers
instrumentation: polarimeters
instrumentation: spectrographs
light pollution
methods: analytical
methods: data analysis
methods: laboratory: atomic
methods: laboratory: molecular
methods: laboratory: solid state
methods: miscellaneous
methods: numerical
methods: observational
methods: statistical
site testing
space vehicles
space vehicles: instruments
techniques: high angular resolution
techniques: image processing
techniques: imaging spectroscopy
techniques: interferometric
techniques: miscellaneous
techniques: photometric
techniques: polarimetric
techniques: radar astronomy
techniques: radial velocities
techniques: spectroscopic
telescopes

Astronomical data bases
astronomical data bases: miscellaneous
atlases
catalogues
surveys
virtual observatory tools

Software
software: data analysis
software: development
software: documentation
software: public release
software: simulations

Astrometry and celestial mechanics
astrometry
celestial mechanics
eclipses
ephemerides
occultations
parallaxes
proper motions
reference systems
time

The Sun
Sun: abundances
Sun: activity
Sun: atmosphere
Sun: chromosphere
Sun: corona
Sun: coronal mass ejections (CMEs)
Sun: evolution
Sun: faculae, plages
Sun: filaments, prominences
Sun: flares
Sun: fundamental parameters
Sun: general
Sun: granulation
Sun: helioseismology
Sun: heliosphere
Sun: infrared
Sun: interior
Sun: magnetic fields
Sun: oscillations
Sun: particle emission
Sun: photosphere
Sun: radio radiation
Sun: rotation
(Sun:) solar–terrestrial relations
(Sun:) solar wind
(Sun:) sunspots
Sun: transition region
Sun: UV radiation
Sun: X-rays, gamma-rays

Planetary systems
comets: general

comets: individual: . . .
Earth
interplanetary medium
Kuiper belt: general

Kuiper belt objects: individual: . . .
meteorites, meteors, meteoroids
minor planets, asteroids: general
minor planets, asteroids: individual: . . .
Moon
Oort Cloud
planets and satellites: atmospheres
planets and satellites: aurorae
planets and satellites: composition
planets and satellites: detection
planets and satellites: dynamical evolution and stability
planets and satellites: formation
planets and satellites: fundamental parameters
planets and satellites: gaseous planets
planets and satellites: general

planets and satellites: individual: . . .
planets and satellites: interiors
planets and satellites: magnetic fields
planets and satellites: oceans
planets and satellites: physical evolution
planets and satellites: rings
planets and satellites: surfaces
planets and satellites: tectonics
planets and satellites: terrestrial planets
planet–disc interactions
planet–star interactions
protoplanetary discs
zodiacal dust

Stars
stars: abundances
stars: activity
stars: AGB and post-AGB
stars: atmospheres
(stars:) binaries *(including multiple)*: close
(stars:) binaries: eclipsing
(stars:) binaries: general
(stars:) binaries: spectroscopic
(stars:) binaries: symbiotic
(stars:) binaries: visual
stars: black holes
(stars:) blue stragglers
(stars:) brown dwarfs
stars: carbon
stars: chemically peculiar
stars: chromospheres
(stars:) circumstellar matter
stars: coronae
stars: distances
stars: dwarf novae
stars: early-type
stars: emission-line, Be
stars: evolution
stars: flare
stars: formation
stars: fundamental parameters
(stars:) gamma-ray burst: general
(stars:) **gamma-ray burst: individual: . . .**
stars: general
(stars:) Hertzsprung–Russell and colour–magnitude diagrams
stars: horizontal branch
stars: imaging
stars: individual: . . .
stars: interiors

stars: jets
stars: kinematics and dynamics
stars: late-type
stars: low-mass
stars: luminosity function, mass function
stars: magnetars
stars: magnetic field
stars: massive
stars: mass-loss
stars: neutron
(stars:) novae, cataclysmic variables
stars: oscillations *(including pulsations)*
stars: peculiar *(except chemically peculiar)*
(stars:) planetary systems
stars: Population II
stars: Population III
stars: pre-main-sequence
stars: protostars
(stars:) pulsars: general
(stars:) **pulsars: individual: . . .**
stars: rotation
stars: solar-type
(stars:) starspots
stars: statistics
(stars:) subdwarfs
(stars:) supergiants
(stars:) supernovae: general
(stars:) **supernovae: individual: . . .**
stars: variables: Cepheids
stars: variables: Scuti
stars: variables: general
stars: variables: RR Lyrae
stars: variables: S Doradus
stars: variables: T Tauri, Herbig Ae/Be
(stars:) white dwarfs
stars: winds, outflows
stars: Wolf–Rayet

Interstellar medium (ISM), nebulae
ISM: abundances
ISM: atoms
ISM: bubbles
ISM: clouds
(ISM:) cosmic rays
(ISM:) dust, extinction
ISM: evolution
ISM: general
(ISM:) HII regions
(ISM:) Herbig–Haro objects

ISM: individual objects: . . .
(except planetary nebulae)
ISM: jets and outflows
ISM: kinematics and dynamics
ISM: lines and bands
ISM: magnetic fields
ISM: molecules
(ISM:) photodissociation region (PDR)
(ISM:) planetary nebulae: general
(ISM:) **planetary nebulae: individual: . . .**
ISM: structure
ISM: supernova remnants

The Galaxy
Galaxy: abundances
Galaxy: bulge
Galaxy: centre
Galaxy: disc
Galaxy: evolution
Galaxy: formation
Galaxy: fundamental parameters
Galaxy: general
(Galaxy:) globular clusters: general
(Galaxy:) **globular clusters: individual: . . .**
Galaxy: halo
Galaxy: kinematics and dynamics
(Galaxy:) local interstellar matter
Galaxy: nucleus
(Galaxy:) open clusters and associations: general
(Galaxy:) **open clusters and associations: individual: . . .**
(Galaxy:) solar neighbourhood
Galaxy: stellar content
Galaxy: structure

Galaxies
galaxies: abundances
galaxies: active
galaxies: bar
(galaxies:) BL Lacertae objects: general
(galaxies:) **BL Lacertae objects: individual: . . .**
galaxies: bulges
galaxies: clusters: general

galaxies: clusters: individual: . . .
galaxies: clusters: intracluster medium
galaxies: disc
galaxies: distances and redshifts
galaxies: dwarf
galaxies: elliptical and lenticular, cD
galaxies: evolution
galaxies: formation
galaxies: fundamental parameters
galaxies: general
galaxies: groups: general

galaxies: groups: individual: . . .
galaxies: haloes
galaxies: high-redshift

galaxies: individual: . . .
galaxies: interactions
(galaxies:) intergalactic medium
galaxies: irregular
galaxies: ISM
galaxies: jets
galaxies: kinematics and dynamics
(galaxies:) Local Group
galaxies: luminosity function, mass function
(galaxies:) Magellanic Clouds
galaxies: magnetic fields
galaxies: nuclei
galaxies: peculiar
galaxies: photometry
(galaxies:) quasars: absorption lines
(galaxies:) quasars: emission lines
(galaxies:) quasars: general

(galaxies:) **quasars: individual: . . .**
(galaxies:) quasars: supermassive black holes
galaxies: Seyfert
galaxies: spiral
galaxies: starburst
galaxies: star clusters: general

galaxies: star clusters: individual: . . .
galaxies: star formation
galaxies: statistics
galaxies: stellar content
galaxies: structure

Cosmology
(cosmology:) cosmic background radiation
(cosmology:) cosmological parameters
(cosmology:) dark ages, reionization, first stars
(cosmology:) dark energy
(cosmology:) dark matter
(cosmology:) diffuse radiation
(cosmology:) distance scale
(cosmology:) early Universe
(cosmology:) inflation
(cosmology:) large-scale structure of Universe
cosmology: miscellaneous
cosmology: observations
(cosmology:) primordial nucleosynthesis
cosmology: theory

Resolved and unresolved sources as a function of wavelength
gamma-rays: diffuse background
gamma-rays: galaxies
gamma-rays: galaxies: clusters
gamma-rays: general
gamma-rays: ISM
gamma-rays: stars
infrared: diffuse background
infrared: galaxies
infrared: general
infrared: ISM
infrared: planetary systems
infrared: stars
radio continuum: galaxies
radio continuum: general
radio continuum: ISM
radio continuum: planetary systems
radio continuum: stars
radio continuum: transients
radio lines: galaxies
radio lines: general
radio lines: ISM
radio lines: planetary systems
radio lines: stars
submillimetre: diffuse background
submillimetre: galaxies
submillimetre: general
submillimetre: ISM
submillimetre: planetary systems
submillimetre: stars
ultraviolet: galaxies
ultraviolet: general
ultraviolet: ISM
ultraviolet: planetary systems
ultraviolet: stars
X-rays: binaries
X-rays: bursts
X-rays: diffuse background
X-rays: galaxies
X-rays: galaxies: clusters
X-rays: general
X-rays: individual: . . .
X-rays: ISM
X-rays: stars

Transients
(transients:) black hole mergers
(transients:) black hole - neutron star mergers
(transients:) fast radio bursts
(transients:) gamma-ray bursts
(transients:) neutron star mergers
transients: novae
transients: supernovae
transients: tidal disruption events